Materials Science & Engineering A 803 (2021) 140726

Contents lists available at ScienceDirect

Materials Science & Engineering A

journal homepage: http://www.elsevier.com/locate/msea

Enhanced strain hardening by bimodal grain structure in carbon nanotube reinforced Al–Mg composites

Xiaowen Fu [a], Ziyun Yu [a], Zhanqiu Tan [a,*], Genlian Fan [a], Pengfei Li [b], Mingju Wang [b], Ding-Bang Xiong [a], Zhiqiang Li [a,**]

[a] State Key Laboratory of Metal Matrix Composites, School of Materials Science and Engineering, Shanghai Jiao Tong University, Shanghai, 200240, China
[b] Changchun Railway Vehicles Co, Ltd, Changchun, 130052, China

ARTICLE INFO

Keywords:
Carbon nanotubes
Aluminum matrix composites
Bimodal grain structure
Strain hardening
Mechanical properties

ABSTRACT

The uniform distribution of carbon nanotubes (CNTs) can lead to severe grain refinement to ultrafine-grained (UFG) regime of Al matrix, resulting in low strain hardening ability, thereby low ductility in CNT/Al composites. To evade this dilemma, CNT/Al–Mg composites with bimodal microstructures were prepared by a powder assembly process in this study. The effects of weight/volume fraction of coarse grains on microstructure evolution, plastic deformation behavior and micro-strain distribution were investigated. The elongation improved from 4.2% of the uniform microstructure to 5.2% for the bimodal CNT/Al–Mg composites with 25 wt% (CG25) coarse grains. The compression stress relaxation test revealed the enhanced effective stress and activation of multiple dislocation-mediated mechanisms during plastic deformation in the CG25 sample, which lead to sustainably higher strain hardening ability. The uniform micro-strain distribution was revealed in the CG25 sample by Kernel average misorientation analysis, attributed to the constrained deformation of soft coarse-grain phase by hard CNT-enriched UFG Al–Mg phase.

1. Introduction

In the field of metal matrix composites (MMCs), carbon nanotubes (CNTs) reinforced aluminum matrix (CNT/Al) composite has been a hot research topic owing to its exceptional mechanical performance and potential application in lightweight design [1,2]. The introduction of high-performance CNTs could not only enhance stiffness and strength, but also reduce weight [3]. However, the CNT/Al composites generally suffered from the problem of unsatisfied ductility, which originated from significant grain refinement down to nano/submicron scale with CNTs addition, weakening strain hardening ability and leading to early strain localization in the Al matrix [4–6]. Thus, how to improve strain hardening ability and retard strain localization was the key to obtain CNT/Al composite with improved ductility and balanced mechanical performance.

Actually, low strain hardening ability and strain localization were universal problems in metals with nanograins or ultrafine grains (NG/UFGs) [7]. To solve the problems, the idea of heterogeneous structure design was proposed [8]. Many novel designs, including bimodal [9], gradient [10], heterogeneous lamella [11] and harmonic structures [12], have been developed to improve ductility/strain hardening ability of NG/UFG metals. Among all these designs, the bimodal design was the most investigated one owing to its simple structure and high effectiveness since its early invention by Wang in 2002 [9]. Inspired by these pioneer works, Lavenia and co-workers tried to improve the ductility of nanostructured MMCs (NMMCs) through the bimodal design of the metal matrix, and proposed the idea of "trimodal" MMCs, which consisted of nano-sized reinforcements, ultrafine grains and coarse grains matrix [13]. Typically, improved ductility and toughness have been achieved through designing such a trimodal structure in B_4C/Al composites. Further investigation revealed that the blunting effect of B_4C/Al and UFG/CG heterogeneous interfaces on crack propagation was key for toughness improvement [14]. Similarly, Esawi and co-works applied bimodal design in CNT/Al composite and achieved increased tensile strength and ductility, attributed to the coordinated roles of hard CNT/Al region and soft Al matrix region in strengthening and toughening respectively [15]. Very recently, Ma and co-works [16] studied heterogeneous CNT/Al–Cu–Mg composites, consisting of CNT-free CG

* Corresponding author.
** Corresponding author.
E-mail addresses: tanzhanqiu@sjtu.edu.cn (Z. Tan), lizhq@sjtu.edu.cn (Z. Li).

https://doi.org/10.1016/j.msea.2020.140726
Received 4 August 2020; Received in revised form 9 December 2020; Accepted 26 December 2020
Available online 30 December 2020

bands and CNT-rich UFG zones, and the reason of considerably enhanced elongation was found to be the greatly suppressed strain localization and the effectively blunted micro-cracks, due to the presence of CG bands.

Actually, no matter how the topology of heterogeneous structures differs, the underlying intrinsic toughening mechanism was generally the same, which was the geometrically necessary dislocations (GNDs) that were required to accommodate the strain gradient between heterogeneous phases. GNDs not only promoted intragranular dislocation accumulation, but also provided long-range internal stress (back stress) hardening to improve strain hardening ability [8,10,11]. However, in the bimodal CNT/Al composites or other NMMCs, research emphasis was still put on revealing the effect of bimodal structure design on the crack nucleation and propagation [14,17], which has been studied in traditional MMCs [18] and was irrelevant with the intrinsic toughening mechanism of bimodal structure for promoting dislocation accumulation and improving strain hardening. In such situation, it is in lack of theoretical guidance for optimizing bimodal structure design and enhancing strain hardening ability of CNT/Al composites. Thus, further studies on revealing the effect of bimodal structure design on dislocation motion and plastic deformation behavior are of great importance.

In the present study, CNT/Al–Mg composites with uniform and bimodal grain structures, were prepared by the powder assembly process. The optical microscope, TEM observation and tensile test have been conducted to characterize the microstructure and mechanical properties of the bimodal CNT/Al–Mg composites. Compression stress relaxation test has been applied to reveal the dislocation motion and plastic deformation behavior. Electron backscattered diffraction has been applied to characterize the microstructure evolution and microstrain distribution. The influence of volume fraction of coarse grains on mechanical performance and deformation behavior was also discussed, which could provide insights for optimizing the bimodal structure design in high-performance NMMCs.

2. Materials and experiments

2.1. Raw materials and composite fabrication

Al–Mg alloy powders (5083Al, about 4 wt% Mg, 0.5 wt% Mn and 0.1 wt% Cr for the main alloying elements) with an average particle size of 10 μm were used as the matrix material. Multi-walled CNTs (99.9% in purity fabricated via catalytic vapor deposition from Cnano Tech. Co., Ltd., China) of ~30 nm in diameter and 10 μm in length were used as the reinforcement. The CNT content of CNT/Al–Mg composite was chosen as 1.5 wt% with the consideration of achieving both uniform CNTs dispersion and evident strengthening effect. To achieve the bimodal design and tailor the microstructure, a powder assembly processing route was developed and applied to fabricate CNT/Al–Mg composites. The corresponding schematic diagram was shown in Fig. 1.

The fabrication process mainly consists of five steps. Step 1 and 2 are the preparation of CNT/Al–Mg composite powders (with CNT content of 1.5 wt%, 2 wt% and 3 wt%) by shift-speed ball milling, including low-speed ball milling and high-speed ball milling [19]. Step 3 is the mechanical blending of as-prepared CNT/Al–Mg composite powders and raw Al–Mg alloy powders. In this way, bimodal structure design was achieved by introducing the coarse grains phases (raw Al–Mg alloy powders) into NG/UFGs phases (severely deformed CNT/Al–Mg composite powders). To keep the total CNT content as 1.5 wt% and achieve bimodal structure design with different coarse grain fraction, the 2 wt% CNT/Al–Mg composite powders and raw Al–Mg alloy powders were mixed with a weight ratio of 3:1 (denoted as CG25, CG stands for coarse-grain), while the 3 wt% CNT/Al–Mg composite powders and raw Al–Mg alloy powders were mixed with the ratio of 1:1 (denoted as CG50). Step 4 and 5 aim to the densification of as-mixed composite powders through compaction, sintering and extrusion. The powder compact was sintered at 510 °C for 2 h and then extruded at 450 °C with an extrusion ratio of 25:1. For comparative study, the 1.5 wt% CNT/Al–Mg composites with uniform microstructure (denoted as CG0) and Al–Mg alloy without CNTs were also prepared by the same process.

2.2. Material characterizations and mechanical tests

Raman spectrum (Senterra R200-L, Bruker) was applied to identify the structures of CNTs. Optical microscope (ZEISS Smartproof 5), scanning electron microscopy (SEM, Tescan Mira3) equipped with electron backscattered diffraction (EBSD) and transmission electron microscopy (TEM, JOEL 2100F) were applied to reveal the microstructures of CNT/Al–Mg composites. The samples for optical microscope were mechanically polished by Struers Tegramin-25 and then etched by Kohler reagent for 10 s. The samples for EBSD characterization were

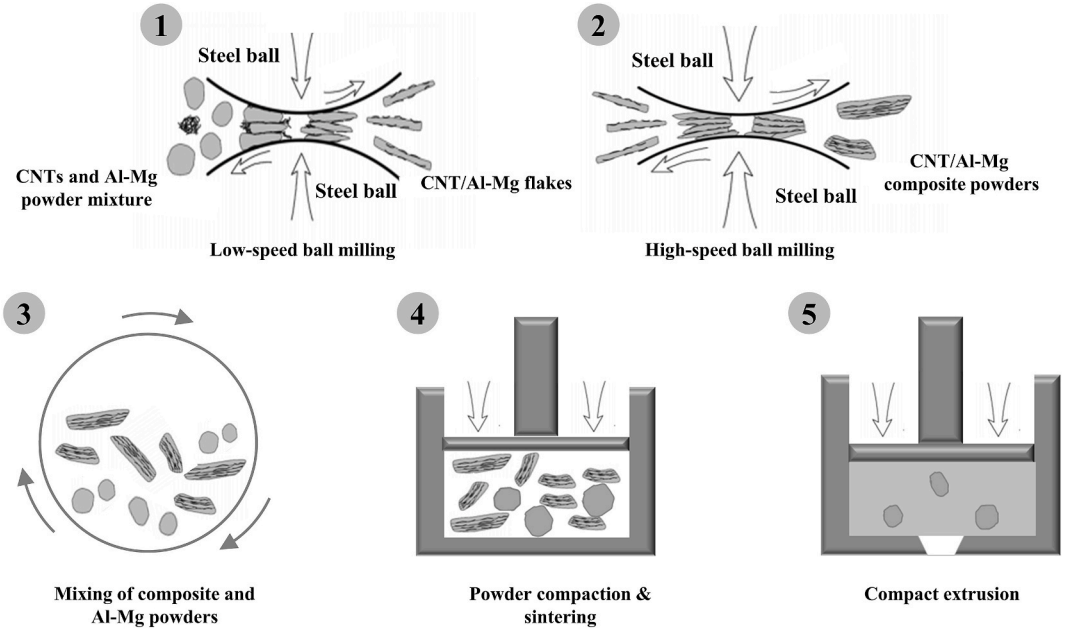

Fig. 1. Schematic diagram of fabricating bimodal CNT/Al–Mg composites by powder assembly.

prepared by mechanical polishing and followed by ion polishing. The TEM samples were thin foil discs with 3 mm diameter and were prepared by ion-milling. The X-ray diffraction (XRD) analysis was carried out using a Rigaku D/Max-2500 X-ray diffractometer with Cu Kα (λ = 0.15406 nm) radiation. The crystallite sizes and lattice strains of CNT/Al–Mg powders were determined from the full width at half maximum (FWHM) of diffraction peaks by Williamson and Hall method [20]. To evaluate the material's mechanical property, dog-bone shaped specimens were machined from extruded rods with a gauge length of 20 mm and a diameter of 4 mm for tensile test at the strain rate of $5 \times 10^{-4}\ s^{-1}$, using a universal testing machine (Zwick-100). Cylindrical pillars of 2 mm in diameter and 4 mm in height with the long axis parallel to extrusion direction were wire-cut from the extruded bar. Stress relaxation compression test was conducted on the as-prepared pillars using Instron 3344 universal testing machine at the strain rate of $5 \times 10^{-4}\ s^{-1}$. One complete progressive relaxation test consists of 10 cycles of compression stress relaxation tests, which were conducted at every 0.5% engineering strain for 90s within the strain range of 0–5%. At least three specimens were tested under each condition to get the statistics for all mechanical tests.

3. Results and discussion

3.1. Microstructure of CNT/Al–Mg powders

Fig. 2a–c shows CNT distributions on the surface of CNT/Al–Mg powders with different CNT content after low-speed ball milling. It can be seen that the CNTs are uniformly dispersed, and the number of CNT on the surface gradually increases with increasing CNT content. Fig. 2d–f shows the morphology of CNT/Al–Mg powders after high-speed ball milling, all the powders are cold welded into particles, but the particle size is different. With the increase of CNT content, the particle size gradually decreases from 52 μm of particles with 1.5 wt% CNT to 32 μm of particles with 3 wt% CNT. Therefore, it can be considered that the increase of CNT content can reduce the particle size of CNT/Al–Mg powders. M. Yazdan Mehr et al. [21] also found the same phenomenon during the ball milling of Ni_3Al-xB-1wt% CNT ($0.0 < x < 1.5$ at%), which was believed to be related to the lattice distortion and increased energy adsorption induced by CNT introduction to the matrix. To further verify this statement, Table 1 shows the lattice strains and crystallite sizes of CNT/Al–Mg composite powders with different CNT content. It's found that the lattice strain does increase with increasing CNT content, further confirming this explanation. Moreover, increasing CNT content not only decreases particle size but also decreases grain size of powders, which should be attributed to the pinning effect of CNT on the grain boundary [22].

3.2. Microstructure of CNT/Al–Mg composites

As shown in Fig. 3a, the dark image contrast indicates the polished surface of the CG0 sample is uniformly etched and the grain sizes are similar. In comparison, for CG25 sample in Fig. 3b, distinct and uniformly distributed bright and dark zones are observed. The dark zones correspond to the fine grain zones due to faster etching rate with more grain boundaries, while the bright zones correspond to the coarse grain zones due to slower etching rate with fewer grain boundaries. For CG50 sample in Fig. 3c, the area fraction of bright zone is larger than that of CG25 sample, which is attributed to its larger weight fraction (50 wt%) of raw Al–Mg alloy powders. In Fig. 3d, e and f, from the view parallel to extrusion direction, typical extrusion structure can be observed with elongated grains aligned along the extrusion direction. In addition, bimodal grain structure with distinct bright and dark zones can also be observed. It's easily understood that the coarse and fine grains originate from the mixed raw Al–Mg alloy powders and the milled composite powders, respectively. The elongated coarse grains were formed by the extrusion of the raw Al–Mg alloy powders. However, the milled CNT/Al–Mg composite powders underwent severe deformation during ball milling, leading to significant grain refinement to form the fine grains. These fine grains would be retained under the confinement of CNTs

Table 1
Crystallite size and lattice strains of CNT/Al–Mg composite powders with different CNT content.

Powders	1.5 wt%	2 wt%	3 wt%
Grain size (nm)	77.6	65.4	60.1
Lattice strain	0.12	0.13	0.14

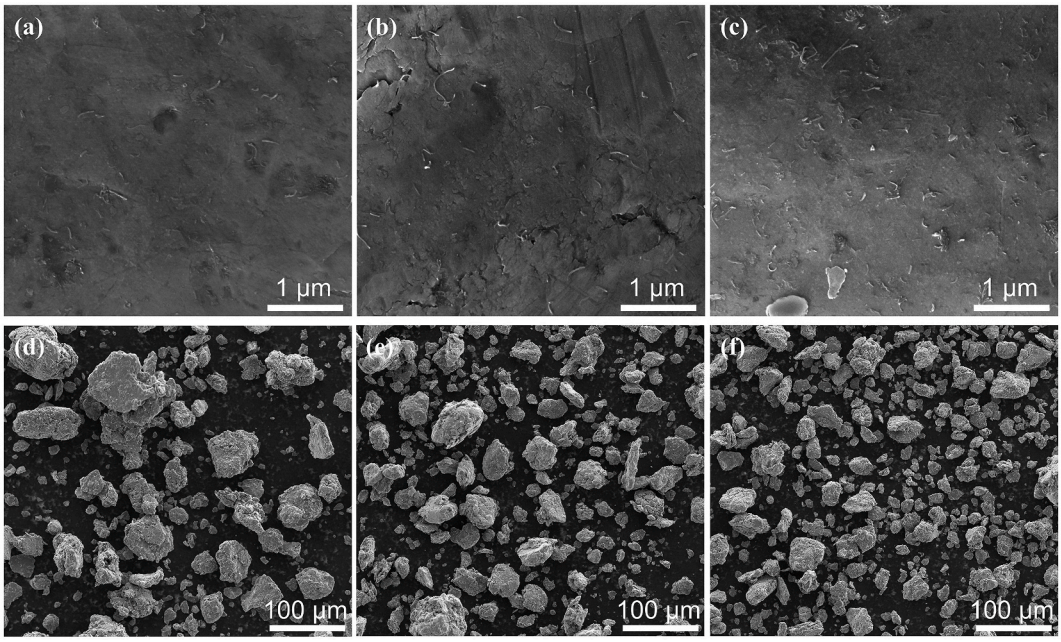

Fig. 2. SEM images showing the CNT distributions after low-speed ball milling and powder morphology after high-speed ball milling of CNT/Al–Mg powders with different CNT content: (a, d) 1.5 wt%, (b, e) 2 wt% and (c, f) 3 wt%.

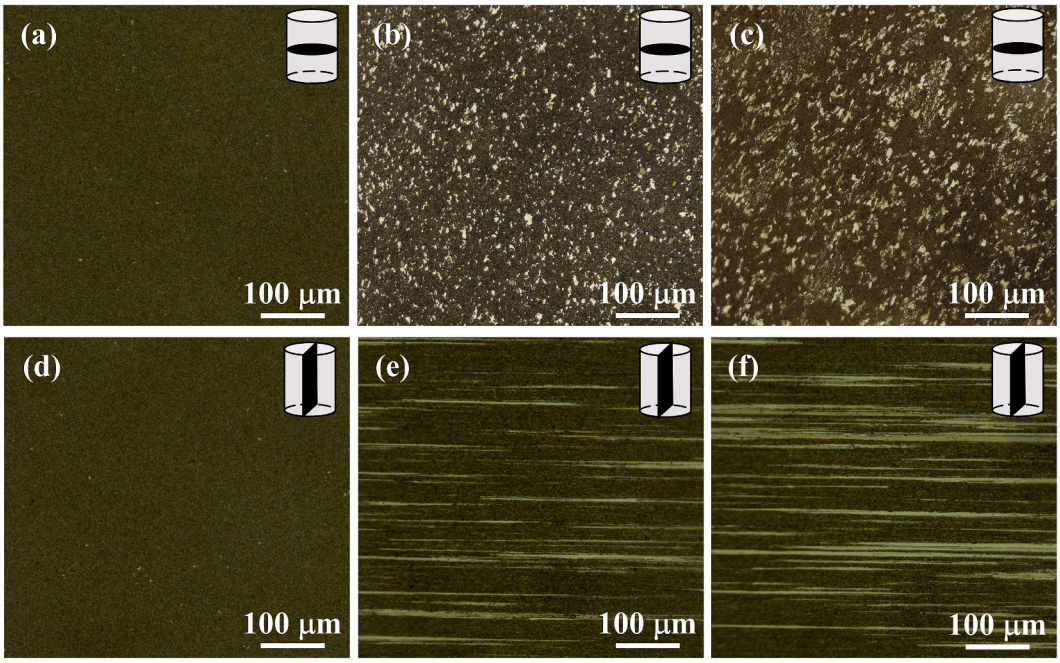

Fig. 3. Optical images showing the microstructure of etched CNT/Al–Mg composites in (a–c) the transverse direction and (d–f) the vertical direction: (a, d) CG0, (b, e) CG25 and (c, f) CG50.

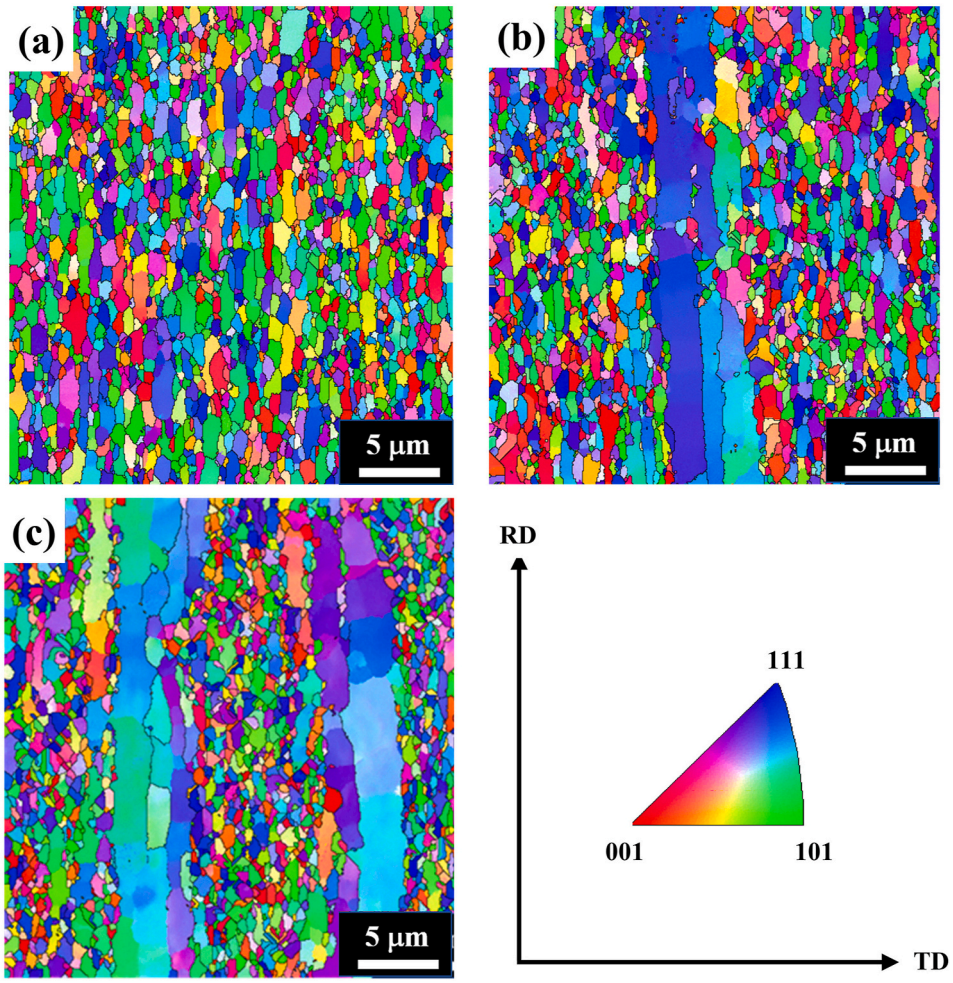

Fig. 4. EBSD images showing the grain structure of (a) CG0, (b) CG25 and (c) CG50 CNT/Al–Mg composites.

during the consolidation process. Consequently, the CNTs-enriched fine-grain zones were formed in the bimodal composites. Thus, bimodal grain structure with uniformly distributed fine and coarse grain zones were successfully achieved through the addition of raw Al–Mg alloy powders during the powder assembly process. Seen from the above, all three samples are uniform and well densified on the macroscale. For further analyzing grain size distribution and better revealing bimodal structure features, EBSD tests have been conducted and the results were shown in Fig. 4.

As shown in Fig. 4a, the grains of CG0 sample are generally uniform and slightly elongated along extrusion direction without evident extrusion texture. While, for the CG25 and CG50 samples, significantly elongated coarse grains with long axis length over tens of microns can be observed. A few of elongated coarse grains gather together, forming a long coarse-grain band embedded in the fine-grain zone, which is the typical bimodal grain structure and consistent with the results in Fig. 3. The analysis in Fig. 3 shows that the coarse grains are from the raw Al–Mg alloy powders, while the fine grains are from the ball-milled CNT/Al–Mg powders. Because the raw Al–Mg alloy powders have lower strength and better deformability than the ball-milled CNT/Al–Mg powders, the coarse grains were significantly elongated during the extrusion process. The grain size distributions of all three samples were statistically counted and the results were shown in Fig. 5.

As shown in Fig. 5a–c, most grains in CG0/25/50 samples are UFGs and the average grain sizes are 0.72, 0.68 and 0.63 μm, respectively. Despite the existence of coarse grains, the average grain sizes of CG25 and CG50 samples are even smaller than that of CG0 sample, which should be caused by two reasons. Firstly, coarse grains are high in volume fraction but low in number, which makes it less significant for counting average grain size. Secondly, for CG25 and CG50 samples, the local CNT content in UFG regions is higher than that of CG0 samples (2 wt% and 3 wt% over 1.5 wt%), which lead to the inhibited grain growth and increased fraction of UFG, as shown in Fig. 5b and c. Compared with the count fraction, the area fraction is a more effective indicator for bimodal grain structure, as shown in Fig. 5d–f. In Fig. 5d, typical unimodal distribution is identified in CG0 sample, while bimodal distributions are identified in Fig. 5e and f. In the meantime, CG50 sample shows a higher area fraction of coarse grains than that of CG25 sample, which is consistent with the doubled weight fraction of added raw Al–Mg alloy powder for CG50 sample.

Fig. 6a–c show the TEM images of representative microstructures of CG0, CG25 and CG50 CNT/Al–Mg composites, respectively. The grain structures of different samples show the same trend with the above results. The CNTs are uniformly dispersed in the UFG zones, and no CNTs are observed in the coarse-grained regions. Fig. 6d further shows the spatial distribution of CNTs. It can be seen that the CNTs are mainly distributed at the grain boundaries in UFG regions, which can effectively hider grain growth due to the Zener pinning effect [23]. Therefore, the UFG zones can be retained during consolidation, while the coarse grain without CNTs would grow significantly. The hollow-structured CNTs can be observed clearly in Fig. 6e, and the CNT/Al interfaces are well bonded. To further analyze the structures of CNTs statistically, the Raman spectra results were shown in Fig. 6f. Well-shaped D and G peaks of CNTs were detected around 1360 and 1580 cm^{-1} in all three samples. In the meantime, the intensity ratios of D peak to G peak, which semi-quantitatively represents the quality of CNTs [24], are similar for CG0/25/50 samples (0.97, 0.98 and 0.98, respectively), which is just slightly higher than the value of raw CNTs (0.94). All these facts indicate that the graphite structures of CNTs are well preserved after processing. Seen from the above, bimodal structure design featured with elongated coarse-grain band embedded in CNT/Al–Mg (UFG) regions was successfully achieved, and the local/total CNT content and coarse grain fraction can be well tailored.

3.3. Mechanical property of CNT/Al–Mg composites

The mechanical properties of CNT/Al–Mg composites and Al–Mg alloy were shown in Fig. 7a. Compared with the Al–Mg alloy sample, CG0/25/50 composites show moderate enhanced Young's modulus (E), significantly improved yield strength (YS) and ultimate tensile strength (UTS), indicating good stiffening/strengthening effect of CNTs. Considering that CNTs are mainly located at grain boundaries in this study, the strengthening of CNTs mainly comes from grain refinement [21], load transfer [25] and thermal mismatch [26]. In the meantime,

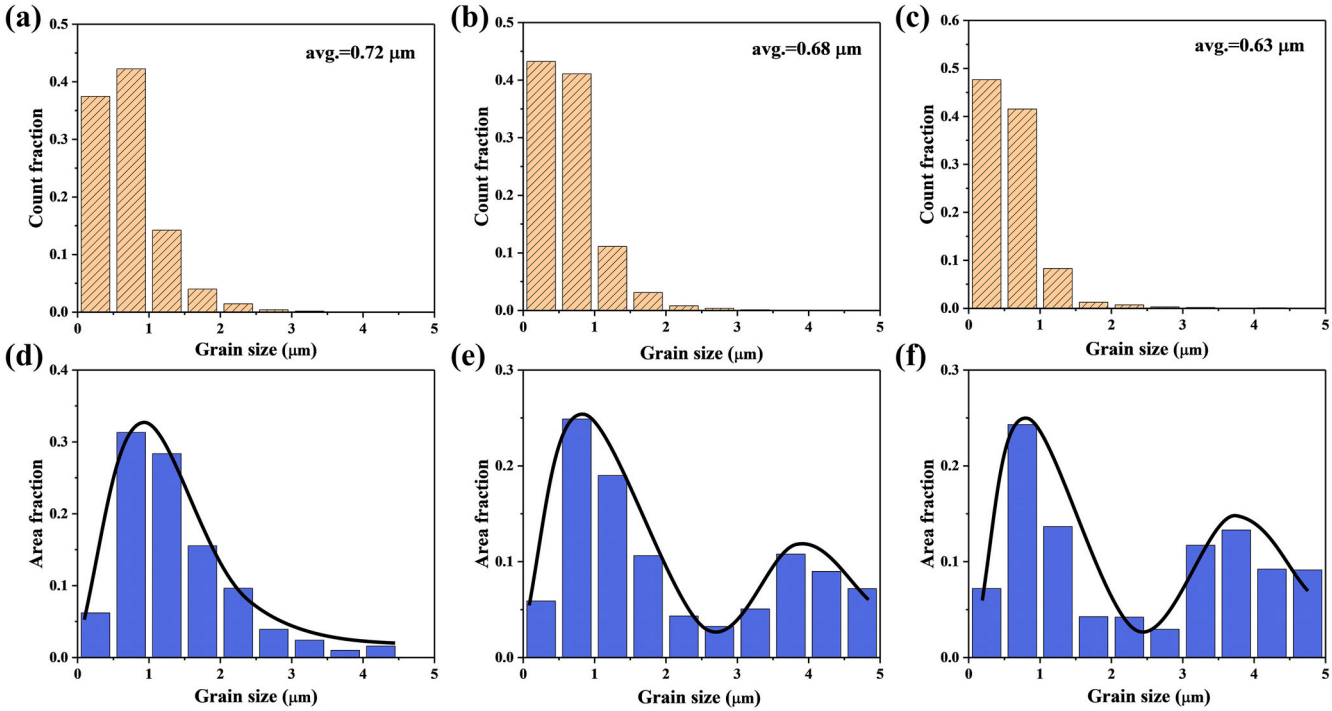

Fig. 5. Count fraction and area fraction of grains with different sizes in (a, d) CG0, (b, e) CG25 and (c, f) CG50 CNT/Al–Mg composites.

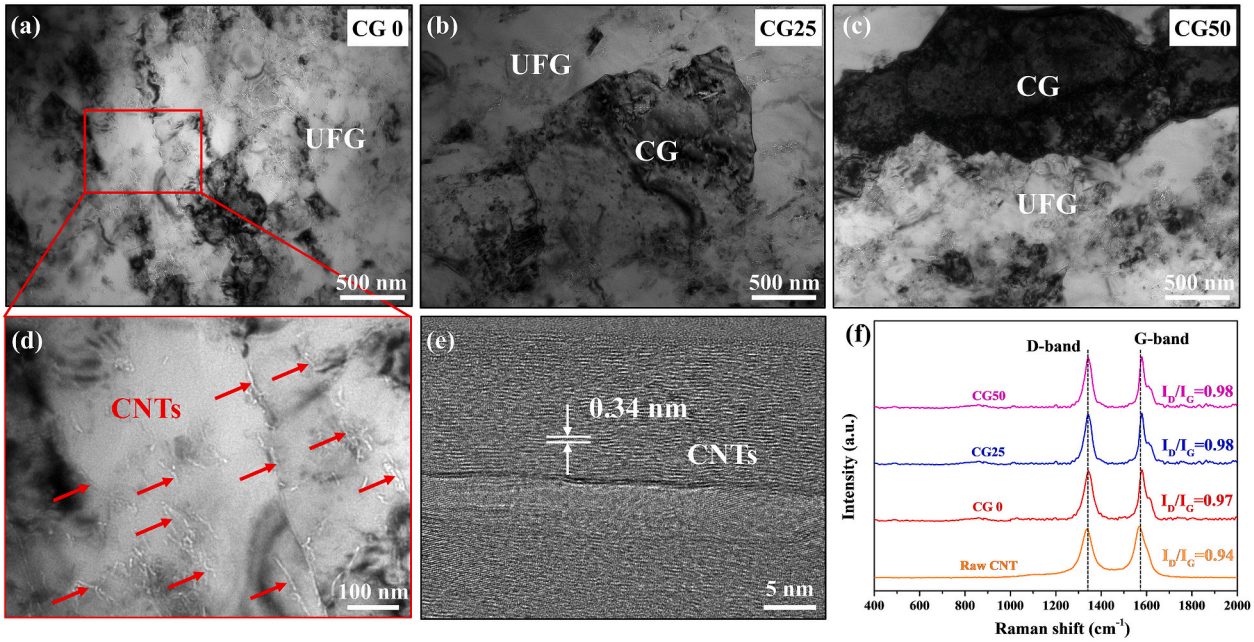

Fig. 6. (a–c) Typical TEM images of CG0, CG25 and CG50 CNT/Al–Mg composites, (d) the enlarged view of the box area in (a), (e) tube structures of CNTs in the UFG zones, (f) Raman spectra of CG0, CG25 and CG50 CNT/Al–Mg composites.

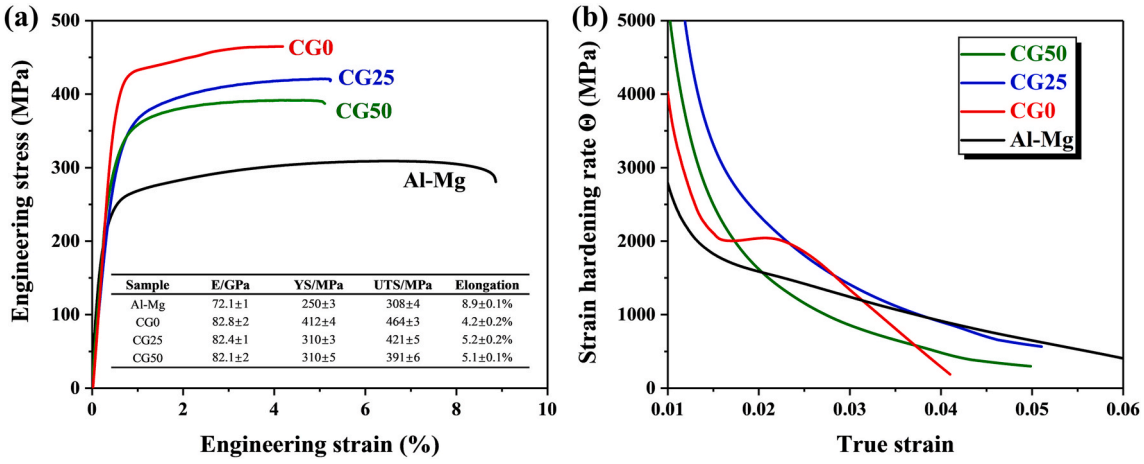

Sample	E/GPa	YS/MPa	UTS/MPa	Elongation
Al-Mg	72.1±1	250±3	308±4	8.9±0.1%
CG0	82.8±2	412±4	464±3	4.2±0.2%
CG25	82.4±1	310±3	421±5	5.2±0.2%
CG50	82.1±2	310±5	391±6	5.1±0.1%

Fig. 7. (a) Engineering tensile stress-strain curves and (b) strain hardening rate curves after 0.01 true strain of Al–Mg alloy and CG0/25/50 CNT/Al–Mg composites.

the elongations of CG0/25/50 composites inevitably decrease from 8.9 ± 0.1% to 4.2 ± 0.2%, 5.2 ± 0.2 and 5.1 ± 0.1%, respectively. The bimodal structure design generally leads to a decrease of YS/UTS, but an increase of elongation. Although both CG25 and CG50 are of bimodal structure design, their mechanical property and plastic deformation behavior are different. Compared with CG50 sample, CG25 sample demonstrates better strain hardening ability and, consequently, higher UTS without sacrificing elongation. For better demonstration, the strain hardening rate ($\Theta = d\sigma/d\varepsilon$, where σ and ε are true stress and true strain, respectively) curves after 0.01 true strain of Al–Mg alloy and CG0/25/50 composites were plotted in Fig. 7b. As can be seen, the CG25 sample shows a sustainably higher strain hardening rate than CG0 and CG50 samples, which achieves the goal of bimodal structure design. However, the effect of bimodal grain structure design is closely dependent on the volume fraction of coarse grains, which is consistent with the results of bimodal structure design in metal and alloys [27], e.g., CG50 sample doesn't improve the strain hardening rate.

3.4. Plastic deformation behavior of CNT/Al–Mg composites

The dislocation motion is the essence of the strain hardening and plastic deformation behavior [28]. Progressive stress relaxation experiments are effective to probe the plasticity behavior of materials due to its sensitivity to dislocation dynamics [29], which could help further reveal the difference of plastic deformation between Al–Mg alloy and CG0/25/50 composites. Fig. 8 shows the progressive stress relaxation cycles of Al–Mg alloy and CG0/25/50 composites. At the initial stage of plastic deformation with stress level under ~75 MPa, all the samples are still in the elastic regime, and no detectable stress decay is observed. However, with increasing stress level and plastic strain, appreciable stress relaxation occurs, and the decay magnitude for each relaxation cycle increases with higher stress levels. Such gradual stress drop is generally thought to be due to the interaction of relaxed dislocation and localized barriers [30], such as dislocation forests and solute atoms, when the total strain of the sample is constant. The applied stress, σ, has two components [31,32]:

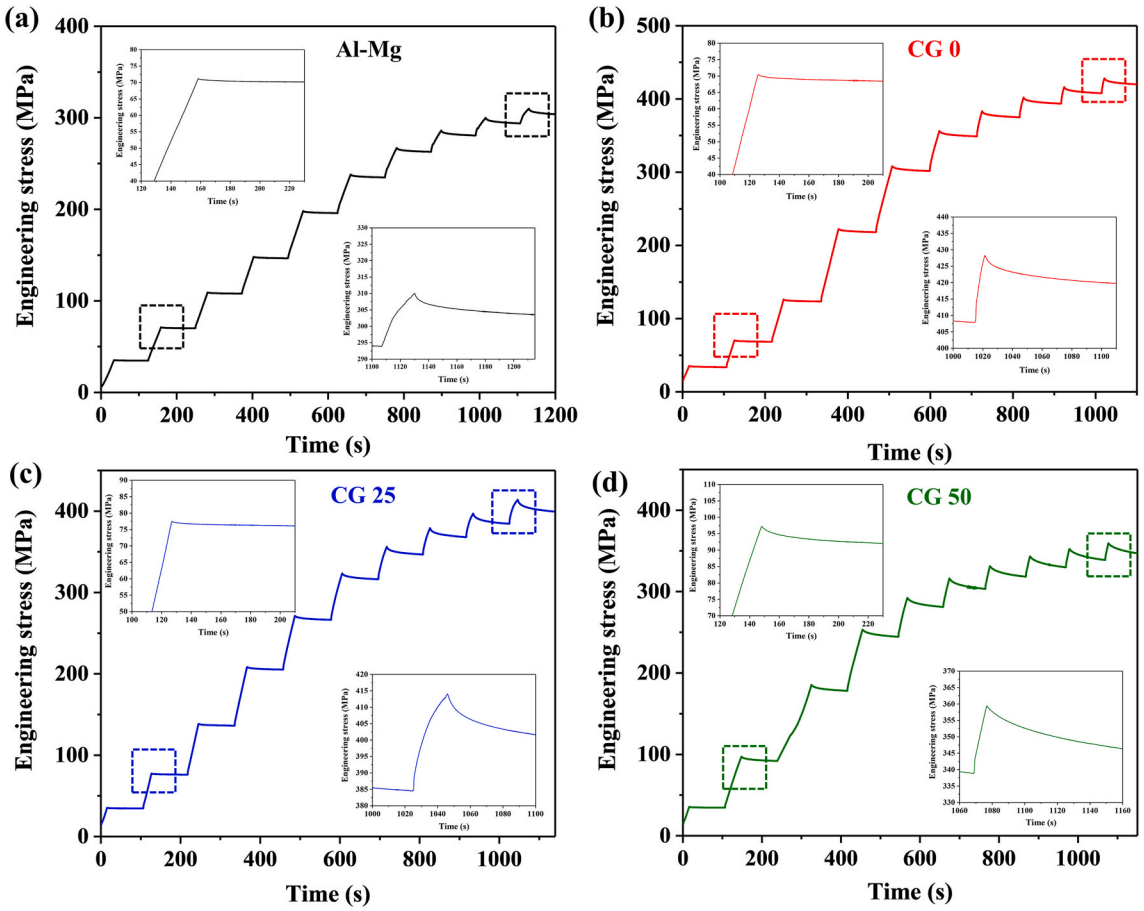

Fig. 8. Progressive stress relaxation curves of (a) Al–Mg, (b) CG0, (c) CG25 and (d) CG50 samples. The loading rate was 5×10^{-4} s^{-1}. The insets show the stress decay segments with 0.5% and 5% strain.

$$\sigma = \sigma^* + \sigma_u \tag{1}$$

where σ^* is the effective stress needed to overcome the short-range barriers, and σ_u is the long-range internal stress that impedes dislocation motion. The relation between the applied stress and the relaxation time Δt can be expressed by an empirical equation [31]:

$$\sigma - \sigma_u = \mathrm{K}(a + \Delta t)^{1/(1-m^*)} = \sigma^* \tag{2}$$

where K, a and m* are constants. Therefore, σ_u and σ^* for each relaxation cycle can be obtained by fitting the corresponding stress relaxation curve with Eq. (2). The resulting σ^* and σ_u for each stress relaxation cycle of Al–Mg alloy and CG0/25/50 composites are demonstrated in Fig. 9a and b. Comparing Al–Mg alloy and CG0 composite, CNTs addition results in a significant increase of long-range internal stress from 255 MPa to 295 MPa at the strain of 5%, which should originate from the enhanced long-range interaction of dislocation with both grain boundary and CNTs. While, for CG25 and CG50 samples, the long-range internal stresses were 229 MPa and 240 MPa, respectively, which were similarly lower than the value of CG0 sample despite with the same weight of CNTs. The reason for this drop should be the introduction of coarse grains and decreased fraction of grain boundary. In Fig. 9b, the CG0/25/50 composites show much higher effective stress compared with that of Al–Mg alloy at the strain of 5%, indicating significantly enhanced intragranular dislocation interaction. For CNT/Al composites, dislocation interaction could be promoted by the introduction of CNTs, which can produce a lot of GNDs around it to impede dislocation gliding [33]. The same phenomenon was also found in graphene reinforced Al matrix composites [34]. For CG25 and CG50 composites, the heterogeneous microstructure of bimodal design could also enhance dislocation interaction and increase effective stress. On the one hand, the introduction of coarse grains can improve dislocation storage ability. On the other hand, the heterogeneous structures would produce a sufficient amount of GNDs during the deformation, which not only increases the intragranular dislocation density, helps to increase the effective stress, but also effectively prevents the gliding of mobile dislocation to improve dislocation interaction [35]. However, compared with CG0 composite, only CG25 composite shows even higher and sustainably increasing effective stress, which is the major reason why CG25 sample shows much higher UTS than that of CG50 composite. Such trend is in accordance with the high strain hardening rate observed in Fig. 7b, since enhanced dislocation interaction normally leads to stronger strain hardening ability. In other words, bimodal structure design only works and achieves the goal of enhancing strain hardening ability in CG25 composite.

To explore the reason, the apparent activation volumes for plastic deformation of all samples were calculated, which is an effective indicator for revealing the deformation mechanism. According to theory, a single relaxation event is thermally activated and can also be expressed by logarithmic variation of stress ($\Delta\sigma$) as a function of relaxation time (Δt) [36]:

$$\Delta\sigma = -(\sqrt{3}kt \Big/ V^*)\ln(1 + \Delta t / C_r) \tag{3}$$

where k is the Boltzmann constant and T is the absolute temperature, V^* is the apparent activation volume of plastic deformation, and C_r is the time constant.

As shown in Fig. 9c, the apparent activation volume of all samples decreases with increasing strain, which is attributed to the increased

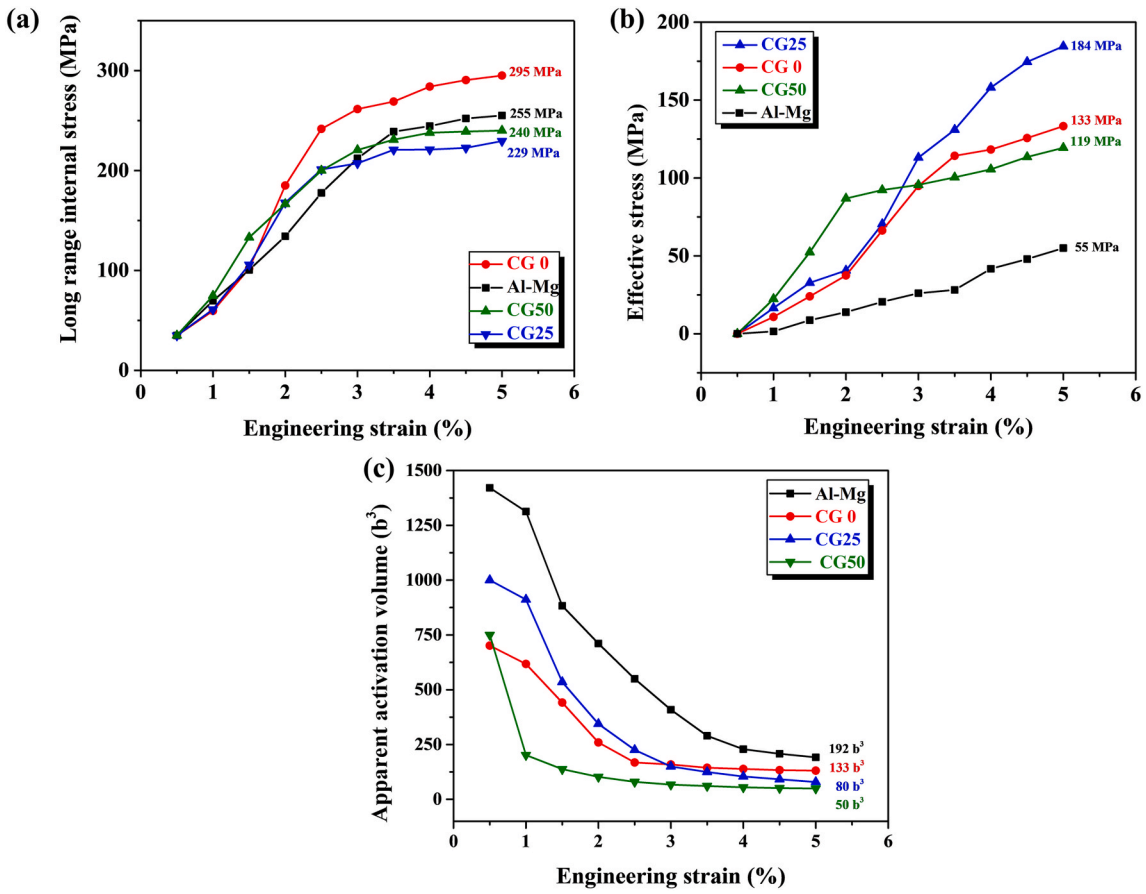

Fig. 9. Evolutions of (a) long-range internal stress, (b) effective stress, (c) plastic deformation apparent activation volume of Al–Mg alloy and CG0/25/50 CNT/Al–Mg composites.

dislocation density and harder dislocation motion [37]. For CG0/25/50 composites, the apparent activation volumes are generally lower than the values of the Al–Mg alloy sample, which should be caused by the stronger short-range dislocation interaction due to the addition of CNTs. Previous studies have also shown that the activation volumes decreased with the increasing CNTs [20]. For Al–Mg alloy and CG0 composite, the apparent activation volumes are higher than 100 b^3 until the strain of 5%, and falls in the same range of forest dislocation cutting mechanism (100–1000 b^3) [38], indicating that their plastic deformation is mediated by dislocation entanglement and forest dislocation cutting throughout the whole deformation process. While, for the CG25 composite, its apparent activation volume becomes lower than 100 b^3 until the strain of 3.5% and ends up as 80 b^3 at the strain of 5%, corresponding to the grain boundary and interface mediated deformation mechanism [36,39]. This means that the CG25 composite fully goes through dislocation entanglement and forest dislocation cutting at the early deformation stage, which could promote intragranular dislocation accumulation and improve strain hardening, and at the later deformation stage, dislocation-grain boundary/interface interactions are activated to further promote dislocation interaction, when the dislocation accumulation is almost saturated. However, for CG50 composite, its apparent activation volume quickly goes down under 100 b^3 at the strain of 1.5%, which means that the ability to accumulate dislocation and strain hardening is soon exhausted at the early deformation stage. Thus, the sustainable ability to accumulate dislocation and activation of multiple deformation mechanisms are the key for CG25 composite to improve effective stress and strain hardening ability.

3.5. *Grain structure and strain distribution of CNT/Al–Mg composite after tensile test*

EBSD characterization has been conducted on the tensile-tested CG0/25/50 CNT/Al–Mg composites, to find out the reason for enhanced dislocation interaction and improved strain hardening in CG 25 composite.

As shown in Fig. 10, compared with the EBSD results before tensile test, the major difference is the appearance of intragranular misorientation in the tested samples, which is caused by the lattice dislocation accommodating for plastic strain during the tensile test. The lattice distortion is more significant for the coarse grains in CG25 and CG50 composites, since the softer coarse grains should deform at a lower strength and bear more strain than the hard CNT/Al–Mg phases. To directly show the strain distribution in the tested samples, Kernel average misorientation (KAM) analysis has been conducted and the results were shown in Fig. 11. With the denoted color shifting from blue to red, the KAM values increasing from 0 to 0.9°, indicating more concentrated local strain [40]. For the CG0 composite, the strain mainly concentrates on the grains with a relatively larger size, while some regions do not bear any strain, which is the typical micro-strain distribution for UFG metals [41]. For the CG25 composite in Fig. 11b, the coarse-grain bands are generally green indicating full participation of coarse grains in the plastic deformation without evident strain localization. In the meantime, the rest CNT/Al–Mg regions demonstrate similar strain distribution with that of CG0 composite. For the CG50 composite, the strain mainly concentrates in the coarse-band and the rest CNT/Al–Mg regions hardly bear any strain, as denoted by the white dashed square.

For better demonstration, image identification on the area fraction of

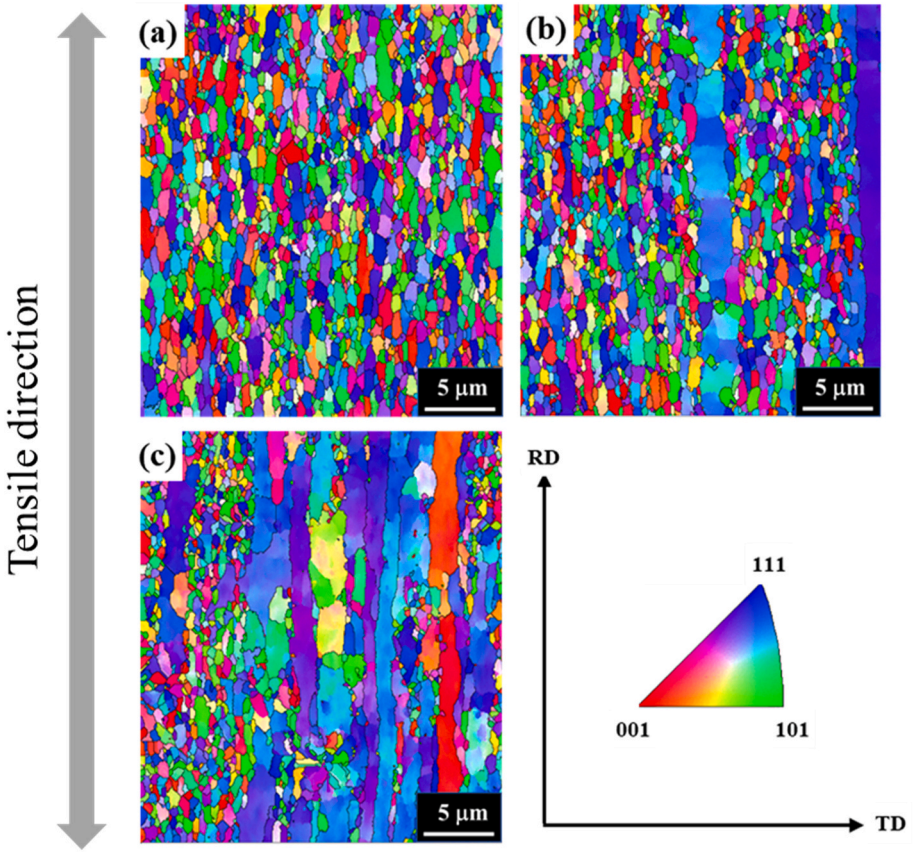

Fig. 10. EBSD images showing the grain structure of (a) CG0, (b) CG25 and (c) CG50 CNT/Al–Mg composites after tensile test.

blue, green and red zones has been conducted, and the results were listed in Table 2. Compared with CG0 composite, the CG25 composite shows a decreased fraction of blue and red zones and an increased fraction of green zone, which indicates that strain distribution is more uniform and an increased fraction of the sample takes part in the plastic deformation. Such results indicate that the original purpose of designing the bimodal structure to avoid strain localization has been achieved to a certain degree. However, for the CG50 composite, the decreased fraction of blue and green zones and increased fraction of red zones indicate that the strain localization is adversely more severe.

The KAM analysis in Fig. 11 also shows the obvious GNDs accumulation in the coarse grains, which is the key to the improved mechanical properties of heterogeneous materials. According to Zhu's study [42], high density of GNDs would be stored at the heterogeneous interface between the coarse-grained region and the UFG region during deformation due to their deformation incompatibility, which forms an interface affected zone (IAZ) with a depth of several microns at the interface. The representative TEM images of fractured CNT/Al–Mg composites in Fig. 12 show the presence of IAZ and its high density of dislocations. The distribution of IAZ in CG25 and CG50 composites is different, the coarse grains in the CG25 sample are basically covered by the IAZ, while the coarse grains in the CG50 sample are only partially covered. The IAZ could improve the work hardening ability through multiple dislocation-mediated mechanisms. First, the heterogeneous interface could act as dislocation sources and sinks to facilitate plastic deformation [43]. Second, the GNDs pile-up in the IAZ could act as forest dislocation to accumulate dislocations [44]. Third, the GNDs pile-up will produce long-range back stress to prohibit further dislocation emission from the dislocation source, improving back stress hardening [45]. As shown in Fig. 12 and demonstrated in Fig. 13, due to the low coarse grain fraction, a higher fraction of coarse grains could be affected by IAZ in CG25 composites compared with that of CG50 composites. Therefore, the multiple dislocation mechanisms facilitated by IAZ could play a major role in CG25 composite, in accordance with the above analysis of activation volume, and enable a higher strain hardening ability and better mechanical performance.

Although both CG25 and CG50 composites are of bimodal structure design and the same CNT content, only CG25 composite demonstrates improved overall mechanical property, better strain hardening ability and moderated strain localization. Such distinct property and plastic deformation behavior should arise from their differences in bimodal structural features. For CG25 composite, the 25 wt% coarse-grain band are surrounded and separated by 75 wt% of the UFG CNT/Al–Mg phases. The early plastic deformation of the soft coarse-grain band should be strongly constrained by the hard CNT/Al–Mg phases, which would result in a complex stress state and promote multiple dislocation slip. As a result, the dislocation accumulation ability in coarse grains is gradually released, resulting in accommodated deformation, sustainable high strain hardening ability and more uniform micro-strain distribution. In such condition, the hard CNT/Al–Mg and soft coarse-grain phases could adequately fulfill the role of strengthening and toughening, respectively. However, the effect of bimodal grain structure design is closely dependent on the volume fraction of coarse grains. For example, for CG50 composite, the weight fraction of coarse grains and CNT/Al–Mg phases are equally 50 wt%, and each phase is spatially connected, which makes the early plastic deformation of soft coarse-grain phase can hardly be constrained by the hard CNT/Al–Mg phase. As a result, the dislocation accumulation ability of coarse grains is quickly consumed and the plastic strain mainly concentrates on the coarse grains. In this case, the hard CNT/Al–Mg and soft coarse-grain phases can hardly fulfill the goal of strengthening and toughening.

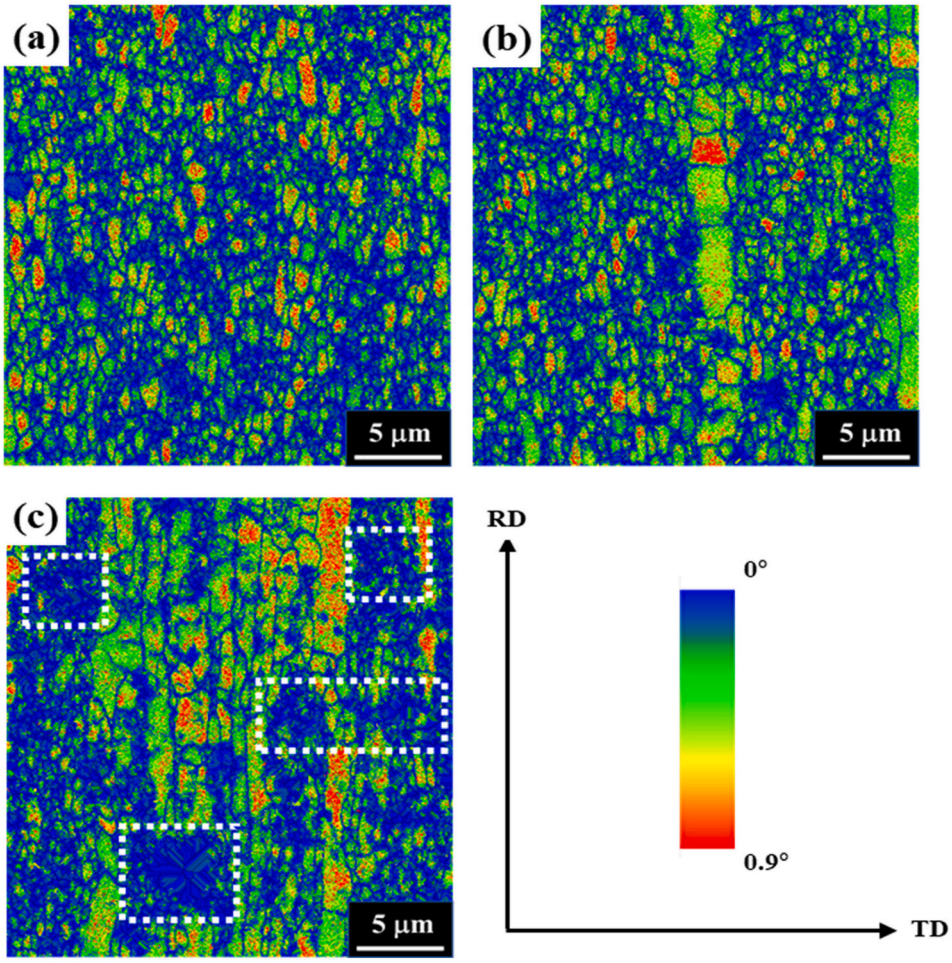

Fig. 11. KAM maps of (a) CG0, (b) CG25 and (c) CG50 CNT/Al–Mg composites after tensile test.

Table 2
Area fraction of micro-zones with different level of strain in CNT/Al–Mg composites.

Sample	Blue Zone	Green Zone	Red zone
CG0	57%	32%	11%
CG25	51%	38%	10%
CG50	55%	31%	14%

4. Conclusions

CNT/Al–Mg composites with bimodal grain structure have been prepared through powder assembly. The effect of weight/volume fraction of coarse grains on microstructure evolution, plastic deformation behavior and micro-strain distribution were investigated. Major results are as follows:

1) For the bimodal CNT/Al–Mg composites, the elongated coarse-grain bands with average grain size over several microns were observed to

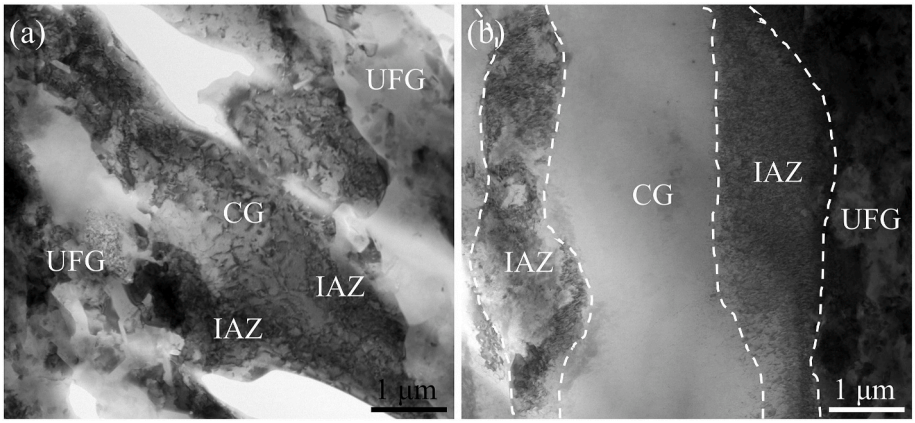

Fig. 12. Typical TEM images of fractured (a) CG25 and (b) CG 50 CNT/Al–Mg composites.

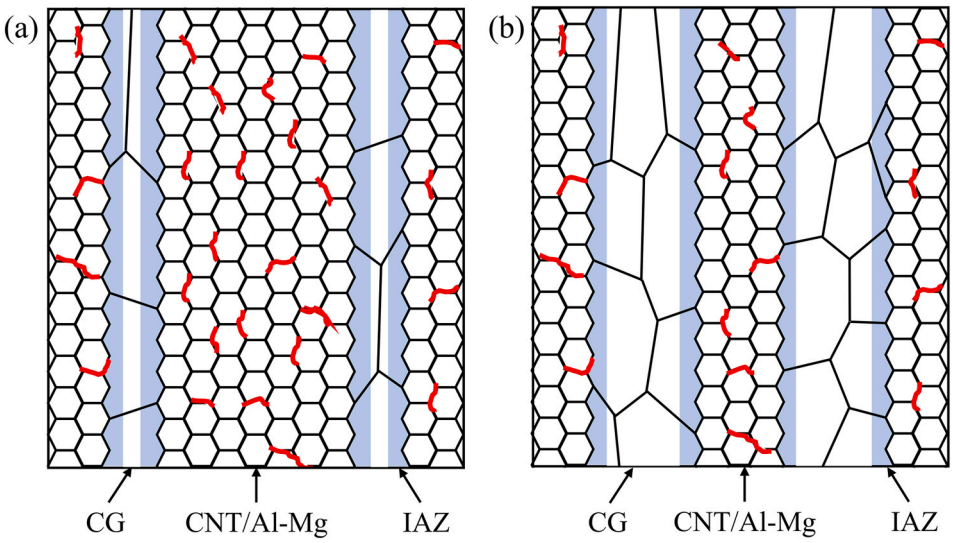

Fig. 13. Schematic of interface affected zone (IAZ) in the coarse grains of (a) CG25 and (b) CG 50 CNT/Al–Mg composites.

be embedded in CNT-enriched UFG Al–Mg regions. With coarse-grain fraction increasing from 25% to 50%, more coarse-grain band can be observed in CG50 sample.

2) The mechanical tests revealed that, for both CG25 and CG50 samples, elongation has improved from 4.2 ± 0.2% to 5.2 ± 0.2% and 5.1 ± 0.1%, while Young's modulus maintained around 82 GPa. However, compared with CG50 sample, the CG25 sample demonstrated the same yield strength but higher ultimate tensile strength, which should be caused by its sustainably higher strain hardening rate after yielding and more uniform micro-strain distribution.
3) The compression stress relaxation test revealed that the enhanced strain hardening ability of CG25 sample originated from the enhancement of effective stress and activation of multiple dislocation-mediated mechanisms during plastic deformation. The uniform micro-strain distribution of CG25 sample was attributed to the constrained deformation of the soft coarse-grain phase by hard CNT-enriched UFG Al–Mg phase. This effect is closely dependent on the volume fraction of coarse grains, and the deformation of the coarse-grain phase can hardly be constrained by hard UFG CNT/Al–Mg phase due to its high volume fraction and spatial connectivity in the CG50 composite. In such case, the plastic strain mainly concentrated in the soft coarse-grain phase, and the hard UFG CNT/Al–Mg was not able to play the role of strengthening.

CRediT authorship contribution statement

Xiaowen Fu: Methodology, Investigation, Visualization, Writing - review & editing. **Ziyun Yu:** Methodology, Investigation, Writing - original draft. **Zhanqiu Tan:** Formal analysis, Investigation, Writing - review & editing. **Genlian Fan:** Project administration, Funding acquisition. **Pengfei Li:** Resources. **Mingju Wang:** Investigation. **Ding-Bang Xiong:** Data curation, Resources. **Zhiqiang Li:** Conceptualization, Supervision, Funding acquisition.

Declaration of competing interest

The authors declare that they have no known competing financial interests or personal relationships that could have appeared to influence the work reported in this paper.

Acknowledgements

This work was supported by the National Key R&D Program of China (No. 2017YFB1201105), the National Natural Science Foundation of China (Nos. 51671130, 51871149, 51971206), the Innovation Foundation of Shanghai Aerospace Science and Technology (No. SAST2018-064), Shanghai Science and Technology Committee (No. 19ZR1474900), and Aeronautical Science Foundation of China (No. 2017ZF57023). We also thank the financial supports from the Administrative Committee of Maanshan Economic and Technological Development Zone, and Jiangsu Province Key Laboratory of High-end Structural Materials (hsm1803).

References

[1] I.A. Ovid'ko, R.Z. Valiev, Y.T. Zhu, Review on superior strength and enhanced ductility of metallic nanomaterials, Prog. Mater. Sci. 94 (2018) 462–540.
[2] M. Jagannatham, P. Chandran, S. Sankaran, P. Haridoss, N. Nayan, S.R. Bakshi, Tensile properties of carbon nanotubes reinforced aluminum matrix composites: a review, Carbon 160 (2020) 14–44.
[3] S.R. Bakshi, D. Lahiri, A. Agarwal, Carbon nanotube reinforced metal matrix composites - a review, Int. Mater. Rev. 55 (1) (2010) 41–64.
[4] D.H. Nam, S.I. Cha, B.K. Lim, H.M. Park, D.S. Han, S.H. Hong, Synergistic strengthening by load transfer mechanism and grain refinement of CNT/Al–Cu composites, Carbon 50 (7) (2012) 2417–2423.
[5] K.T. Kim, J. Eckert, S.B. Menzel, T. Gemming, S.H. Hong, Grain refinement assisted strengthening of carbon nanotube reinforced copper matrix nanocomposites, Appl. Phys. Lett. 92 (12) (2008) 121901.
[6] C.C. Koch, Optimization of strength and ductility in nanocrystalline and ultrafine grained metals, Scripta Mater. 49 (7) (2003) 657–662.
[7] E. Ma, Instabilities and ductility of nanocrystalline and ultrafine-grained metals, Scripta Mater. 49 (7) (2003) 663–668.
[8] E. Ma, T. Zhu, Towards strength–ductility synergy through the design of heterogeneous nanostructures in metals, Mater. Today 20 (6) (2017) 323–331.
[9] Y. Wang, M. Chen, F. Zhou, E. Ma, High tensile ductility in a nanostructured metal, Nature 419 (6910) (2002) 912–915.
[10] T.H. Fang, W.L. Li, N.R. Tao, K. Lu, Revealing extraordinary intrinsic tensile plasticity in gradient nano-grained copper, Science 331 (6024) (2011) 1587–1590.
[11] X. Wu, M. Yang, F. Yuan, G. Wu, Y. Wei, X. Huang, Y. Zhu, Heterogeneous lamella structure unites ultrafine-grain strength with coarse-grain ductility, P. Natl. Acad. Sci. USA. 112 (47) (2015) 14501.
[12] C. Sawangrat, S. Kato, D. Orlov, K. Ameyama, Harmonic-structured copper: performance and proof of fabrication concept based on severe plastic deformation of powders, J. Mater. Sci. 49 (19) (2014) 6579–6585.
[13] L. Jiang, K. Ma, H. Yang, M. Li, E.J. Lavernia, J.M. Schoenung, The microstructural design of trimodal aluminum composites, JOM 66 (6) (2014) 898–908.
[14] H. Yang, T.D. Topping, K. Wehage, L. Jiang, E.J. Lavernia, J.M. Schoenung, Tensile behavior and strengthening mechanisms in a submicron B4C-reinforced Al trimodal composite, Mater. Sci. Eng., A 616 (2014) 35–43.
[15] K. Morsi, A.M.K. Esawi, P. Borah, S. Lanka, A. Sayed, M. Taher, Properties of single and dual matrix aluminum–carbon nanotube composites processed via spark plasma extrusion (SPE), Mater. Sci. Eng., A 527 (21–22) (2010) 5686–5690.
[16] Z.Y. Liu, K. Ma, G.H. Fan, K. Zhao, J.F. Zhang, B.L. Xiao, Z.Y. Ma, Enhancement of the strength-ductility relationship for carbon nanotube/Al–Cu–Mg nanocomposites by material parameter optimisation, Carbon 157 (2020) 602–613.

[17] Z. Zhang, T. Topping, Y. Li, R. Vogt, Y. Zhou, C. Haines, J. Paras, D. Kapoor, J. M. Schoenung, E.J. Lavernia, Mechanical behavior of ultrafine-grained Al composites reinforced with B4C nanoparticles, Scripta Mater. 65 (8) (2011) 652–655.
[18] G.J. Fan, H. Choo, P.K. Liaw, E.J. Lavernia, Plastic deformation and fracture of ultrafine-grained Al–Mg alloys with a bimodal grain size distribution, Acta Mater. 54 (7) (2006) 1759–1766.
[19] R. Xu, Z. Tan, D. Xiong, G. Fan, Q. Guo, J. Zhang, Y. Su, Z. Li, D. Zhang, Balanced strength and ductility in CNT/Al composites achieved by flake powder metallurgy via shift-speed ball milling, Compos. A: Appl. Sci. Manuf. 96 (2017) 57–66.
[20] X. Fu, R. Xu, C. Yuan, Z. Tan, G. Fan, G. Ji, D.-B. Xiong, Q. Guo, Z. Li, D. Zhang, Strain rate sensitivity and deformation mechanism of carbon nanotubes reinforced aluminum composites, Metall. Mater. Trans. 50 (8) (2019) 3544–3554.
[21] A. Mohammadnejad, A. Bahrami, M. Sajadi, M.Y. Mehr, Spark plasma sintering of Ni3Al-xB-1wt% CNT (0.0 <x <1.5 at%) nanocomposite, J. Alloys Compd. 788 (2019) 461–467.
[22] Z.Y. Liu, B.L. Xiao, W.G. Wang, Z.Y. Ma, Modelling of carbon nanotube dispersion and strengthening mechanisms in Al matrix composites prepared by high energy ball milling-powder metallurgy method, Compos. A: Appl. Sci. Manuf. 94 (2017) 189–198.
[23] Y. Xie, Y. Luo, T. Xia, W. Zeng, J. Wang, J. Liang, D. Zhou, D. Zhang, Grain growth and strengthening mechanisms of ultrafine-grained CoCrFeNiMn high entropy alloy matrix nanocomposites fabricated by powder metallurgy, J. Alloys Compd. 819 (2020) 152937.
[24] B. Guo, Y. Chen, Z. Wang, J. Yi, S. Ni, Y. Du, W. Li, M. Song, Enhancement of strength and ductility by interfacial nano-decoration in carbon nanotube/aluminum matrix composites, Carbon 159 (2020) 201–212.
[25] Z.Y. Liu, B.L. Xiao, W.G. Wang, Z.Y. Ma, Analysis of carbon nanotube shortening and composite strengthening in carbon nanotube/aluminum composites fabricated by multi-pass friction stir processing, Carbon 69 (2014) 264–274.
[26] R. George, K.T. Kashyap, R. Rahul, S. Yamdagni, Strengthening in carbon nanotube/aluminium (CNT/Al) composites, Scripta Mater. 53 (10) (2005) 1159–1163.
[27] L. Zhu, S. Shi, K. Lu, J. Lu, A statistical model for predicting the mechanical properties of nanostructured metals with bimodal grain size distribution, Acta Mater. 60 (16) (2012) 5762–5772.
[28] S. Brandstetter, H. Van Swygenhoven, S. Van Petegem, B. Schmitt, R. Maaß, P. M. Derlet, From micro- to macroplasticity, Adv. Mater. 18 (12) (2006) 1545–1548.
[29] Y.M. Wang, A.V. Hamza, T.W. Barbee, Incipient plasticity in metallic glass modulated nanolaminates, Appl. Phys. Lett. 91 (6) (2007), 061924.
[30] Z. Li, L. Zhao, Q. Guo, Z. Li, G. Fan, C. Guo, D. Zhang, Enhanced dislocation obstruction in nanolaminated graphene/Cu composite as revealed by stress relaxation experiments, Scripta Mater. 131 (2017) 67–71.
[31] J.C. Li, Dislocation dynamics in deformation and recovery, Can. J. Phys. 45 (2) (1967) 493–509.
[32] J. Li, On stress relaxation based on dislocation dynamics, Scripta Metall. 15 (8) (1981) 935–936.
[33] R. Xu, G. Fan, Z. Tan, G. Ji, C. Chen, B. Beausir, D.-B. Xiong, Q. Guo, C. Guo, Z. Li, D. Zhang, Back stress in strain hardening of carbon nanotube/aluminum composites, Mater. Res. Lett. 6 (2) (2017) 113–120.
[34] Y. Jiang, R. Xu, Z. Tan, G. Ji, G. Fan, Z. Li, D.-B. Xiong, Q. Guo, Z. Li, D. Zhang, Interface-induced strain hardening of graphene nanosheet/aluminum composites, Carbon 146 (2019) 17–27.
[35] J. Li, Q. Zhang, R. Huang, X. Li, H. Gao, Towards understanding the structure–property relationships of heterogeneous-structured materials, Scripta Mater. 186 (2020) 304–311.
[36] Y. Wang, A. Hamza, E. Ma, Temperature-dependent strain rate sensitivity and activation volume of nanocrystalline Ni, Acta Mater. 54 (10) (2006) 2715–2726.
[37] Z. Li, H. Wang, Q. Guo, Z. Li, D.B. Xiong, Y. Su, H. Gao, X. Li, D. Zhang, Regain strain-hardening in high-strength metals by nanofiller incorporation at grain boundaries, Nano Lett. 18 (10) (2018) 6255–6264.
[38] T. Zhu, J. Li, A. Samanta, H.G. Kim, S. Suresh, Interfacial plasticity governs strain rate sensitivity and ductility in nanostructured metals, P. Natl. Acad. Sci. USA. 104 (9) (2007) 3031–3036.
[39] L. Zhao, Q. Guo, Z. Li, Z. Li, G. Fan, D.-B. Xiong, Y. Su, J. Zhang, Z. Tan, D. Zhang, Strain-rate dependent deformation mechanism of graphene-Al nanolaminated composites studied using micro-pillar compression, Int. J. Plast. 105 (2018) 128–140.
[40] C.W. Shao, P. Zhang, Y.K. Zhu, Z.J. Zhang, Y.Z. Tian, Z.F. Zhang, Simultaneous improvement of strength and plasticity: additional work-hardening from gradient microstructure, Acta Mater. 145 (2018) 413–428.
[41] H.K. Park, K. Ameyama, J. Yoo, H. Hwang, H.S. Kim, Additional hardening in harmonic structured materials by strain partitioning and back stress, Mater. Res. Lett. 6 (5) (2018) 261–267.
[42] C.X. Huang, Y.F. Wang, X.L. Ma, S. Yin, H.W. Höppel, M. Göken, X.L. Wu, H.J. Gao, Y.T. Zhu, Interface affected zone for optimal strength and ductility in heterogeneous laminate, Mater. Today 21 (7) (2018) 713–719.
[43] X. Ma, C. Huang, J. Moering, M. Ruppert, H.W. Höppel, M. Göken, J. Narayan, Y. Zhu, Mechanical properties of copper/bronze laminates: role of interfaces, Acta Mater. 116 (2016) 43–52.
[44] Y. Zhu, X. Wu, Perspective on hetero-deformation induced (HDI) hardening and back stress, Mater. Res. Lett. 7 (10) (2019) 393–398.
[45] X. Wu, Y. Zhu, Heterogeneous materials: a new class of materials with unprecedented mechanical properties, Mater. Res. Lett. 5 (8) (2017) 527–532.